Control of histidine kinase conformation by an ABC-transporter facilitates need-based activation of antibiotic resistance

Alan Koh[1,2], Marjorie J. Gibbon[1,2], Marc W. Van der Kamp[3], Christopher R. Pudney[1], Susanne Gebhard[1,2]*

[1]Department of Biology and Biochemistry, [2]Milner Centre for Evolution, University of Bath, Claverton Down, Bath, BA2 7AY, United Kingdom; [3]School of Biochemistry, University of Bristol, University Walk, Bristol, BS8 1TD, United Kingdom.

*Corresponding author. Phone: +44 1225 386421; E-mail: s.gebhard@bath.ac.uk

Running title: Kinase control by an ABC-transporter

Keywords: Signal transduction, flux-sensing, antimicrobial peptide, cell envelope stress

ABSTRACT

Bacteria exert close control over gene expression to ensure optimal physiological responses to their environment, balancing metabolic costs against physiological gain. Such careful gene expression can be employed to minimize the fitness cost associated with antibiotic resistance, one of the main counteracting forces working against the spread of resistance. We previously described a novel regulatory logic that enables the cell to directly monitor its need for detoxification capacity. This cost-effective strategy for controlling resistance is achieved via a two-component regulatory system working in a sensory complex with an ABC-transporter, which together act as a flux-sensor where signaling is proportional to transport activity. How this is realized at the molecular level, however, has remained unknown. Using experimentation and computation we here show that the histidine kinase is activated by piston-like displacements in the membrane, which are converted to helical rotations in the catalytic core via an intervening HAMP-like domain. Intriguingly, the transporter was not only required for kinase activation, but also to actively maintain the kinase in its inactive state in the absence of antibiotics. Such slaving of kinase activity to that of the transporter will ensure the complete control required for transport flux-dependent signaling. Moreover, we show that the transporter has evolved to conserve energy by signaling with sub-maximal sensitivity. These results provide the first mechanistic insights into transport flux-dependent signaling to control antibiotic resistance, which also has importance in energy-efficient decision making in bacteria more broadly.

36 **INTRODUCTION**

37 Bacteria have exquisite abilities to physiologically respond to environmental conditions to
38 ensure their survival and proliferation. Decision-making has to balance the benefits of a
39 particular response against the metabolic cost of the associated changes in gene expression.
40 The importance of this is particularly evident in the context of antibiotic resistance, where
41 one of the main counteracting forces working against the development and spread of
42 resistance is the associated cost in fitness (1-3). To minimize this cost, many resistance
43 determinants are tightly regulated and only expressed when the cell experiences an antibiotic
44 attack. This in turn requires that the bacterium is able to accurately determine the severity of
45 this attack and adjust the level of gene expression accordingly. Bacteria employ a host of
46 regulatory systems that can detect extracellular or intracellular information and modulate the
47 expression of a defined set of target genes. In the simplest case, regulation is dependent on
48 the presence or absence of a ligand, e.g. an antibiotic, and this is often thought of as a digital
49 response, where gene expression is either switched ON or OFF. However, many regulatory
50 systems display a much more analog behavior, where the output is gradually dialed up in
51 response to the strength of the input information, allowing a very fine-tuned response.

52 We previously described a new sensory strategy that produces an exquisitely fine-tuned
53 antibiotic resistance response, with three orders of magnitude of output modulation over an
54 input dynamic range of three orders of magnitude (4). This regulatory logic is achieved by a
55 two-component system whose histidine kinase works in a sensory complex with an ABC-
56 transporter (4, 5) (Fig. 1). Such systems are wide-spread among low G+C content Gram-
57 positive bacteria, such as bacilli, lactobacilli, staphylococci, streptococci, enterococci and
58 clostridia (6-11). They are collectively referred to as Bce-like systems and impart resistance
59 against a broad range of cell wall-active peptide antibiotics (12, 13). Based on computational

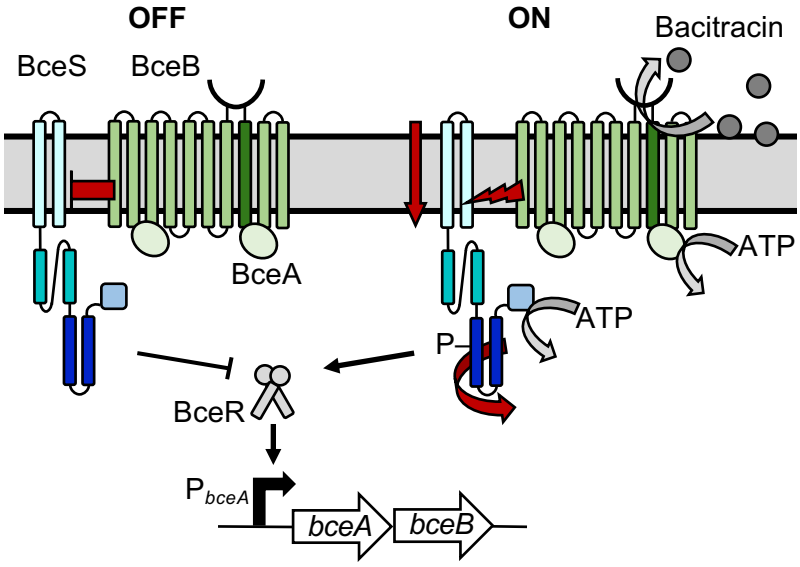

Figure 1. Function of the BceRS-BceAB resistance system of *B. subtilis.* BceS and its domains are shown in shades of blue, with the HAMP-like domain in dark turquoise, and DHp domain in dark blue. Only a single monomer of BceS is shown for clarity. BceAB is in green with the 8th transmembrane helix marked in dark green; the A_2B stoichiometry is shown (5), and the extracellular domain indicated by a U-shaped black line. The left section of the schematic shows the system in its inactive (OFF) state, and the repressing function of the transporter indicated by a red blunt arrow. The right shows the active (ON) state in the presence of antibiotics, exemplified by bacitracin, with the activating function of the transporter shown as a red lightning bolt. The motions of kinase domains upon activation are shown as red block arrows and BceS autophosphorylation by a 'P'. The positioning of the symbols within the sensory complex for repression/activation is arbitrary. ATP hydrolysis reactions and antibiotic removal are indicated by grey arrows; for simplicity ATP hydrolysis is only shown for one ATPase.

60 modelling of the response dynamics, we have established that signaling is proportional to
61 transport activity (4). Because the transporter mediates the actual resistance, presumably by
62 removal of the antibiotic from its target in the cell envelope (4, 14-16), increased transporter
63 production acts a negative feedback on signaling, which creates the characteristic gradual,
64 fine-tuned response (4). This flux-sensing mechanism effectively allows the bacterium to
65 adjust its response according to its need for additional detoxification capacity, implementing
66 a cost-effective 'produce-to-demand' strategy. However, the molecular mechanism of this
67 new signaling strategy, i.e. how the activity of the histidine kinase is controlled within the
68 sensory complex and how this creates the observed analog response behavior, remains
69 unknown.

70 Histidine kinases typically relay extracellular information to the cytoplasm via
71 autophosphorylation at a conserved histidine residue. The phosphoryl group is then
72 transferred to a cytoplasmic response regulator, usually a DNA-binding protein that elicits
73 changes in gene expression (17). Despite their importance in bacterial signaling, we still have
74 limited understanding of the molecular mechanisms by which histidine kinases transmit
75 information through the cytoplasmic membrane. This is in part due to the modular
76 architecture of the kinases, which allows a plethora of different input domains to be coupled
77 to a conserved catalytic core. The core consists of a DHp (also known as HisKA) domain that
78 facilitates dimerization and histidine phosphotransfer, and a C-terminal ATPase domain (17).
79 The extracellular input and cytoplasmic core domains are separated by transmembrane
80 segments and usually at least one cytoplasmic signal transfer domain (e.g. HAMP or PAS
81 domains) (17, 18). While we still have no knowledge of the complete set of conformational
82 changes during transmembrane signaling by histidine kinases, recent studies of domains in
83 isolation or in context with an adjacent domain suggest a combination of rotating and
84 scissoring motions and piston-like helical displacements (18-21).

85 In addition to the diversity of input domains, several kinases are controlled by accessory
86 proteins, providing further levels of control and opportunities for integration of multiple
87 stimuli. In many cases, these accessory proteins are transporters (22, 23). The majority of
88 transporters with a signaling role act as repressors of kinase activity, and deletion of the
89 transporter leads to constitutive activation of signaling (24-26). The paradigm example is the
90 control of the phosphate starvation response in *E. coli* and many other bacteria by the
91 phosphate uptake system PstSCAB, which prevents signaling by the PhoBR two-component
92 system under high-phosphate conditions (26). The flux-sensing Bce-like systems are unique
93 in that the histidine kinases fully rely on their cognate transporters for activation, and remain
94 inactive when the transporter is deleted (12, 27). Moreover, implementing the reported flux-
95 sensing strategy requires kinase activity to be directly proportional to transport activity (4).
96 To our knowledge, no information is available on how accessory proteins may achieve such
97 positive and precise control over a histidine kinase.

98 In the present study, we sought to understand the mechanistic basis of histidine kinase
99 activation in the Bce system of *Bacillus subtilis* and how this links to the system's analog
100 signaling behavior. Through computational predictions, detailed mutagenesis and cysteine
101 cross-linking and accessibility analyses, we provide evidence that the kinase BceS is
102 activated via helical rotations in the DHp domain, accompanied by a piston movement in the
103 second transmembrane domain. Physical motions are most likely relayed via a poorly-
104 conserved intervening HAMP-like domain. To our knowledge this is the first report of a
105 complete set of conformational changes *in vivo* during activation of a membrane-bound
106 histidine kinase. Artificial activation of the kinase through charge substitutions in the DHp
107 domain revealed that the transporter not only acts as the activator of the kinase, but also
108 controls its inactive state. We propose it is this complete control over kinase conformation
109 that slaves its activity to that of the transporter. Surprisingly, mutagenesis of the putative

110 signaling domain of the transporter, BceAB, highlighted that the system has not evolved for
111 maximal signaling sensitivity, which likely represents an additional layer of fine-tuning and
112 minimizing energy expenditure in control of antibiotic resistance.

113

114 **RESULTS**

115 **Generation and validation of a BceS homology model.** Analysis of the domain architecture
116 of BceS using SMART (28) showed two N-terminal transmembrane helices, predicted to end
117 at residue F55, and a prototypical cytoplasmic kinase core with a DHp domain from residues
118 E115 to I172 and ATPase domain from S216 to N326. The 60 amino acid linker between the
119 transmembrane and DHp domains contained no predicted domains. To investigate the
120 cytoplasmic composition of BceS in more detail, we used I-TASSER (29) to predict the
121 tertiary structure of the linker region and DHp domain (residues R56 to N174; Fig. 2a). The
122 closest structural analog was the hybrid kinase Af1503-EnvZ from *Archaeoglobus fulgidus*
123 and *E. coli*, respectively (PDB 3ZRW). BceS showed the typical DHp domain fold of two
124 antiparallel helices (DHp1 and DHp2), joined by a short loop. In the functional kinase dimer,
125 this will form the four-helix bundle characteristic for most histidine kinases (17) (Fig.2c).
126 Interestingly, the linker between the membrane interface and DHp domain adopted a HAMP-
127 like conformation with two short parallel helices (HAMP-like 1 and HAMP-like 2), where
128 HAMP-like 2 continues into DHp1 as a single continuous helix (Fig. 2a). The relevance of
129 this domain, which had not been predicted in previous analyses, is discussed in more detail
130 below.

131 To test the accuracy of the homology model, we probed the relative orientation of helices
132 within the DHp domain four-helix bundle, based on proximity of individual residues, using
133 oxidative cysteine crosslinking. These experiments were done *in vivo* using cells deleted for

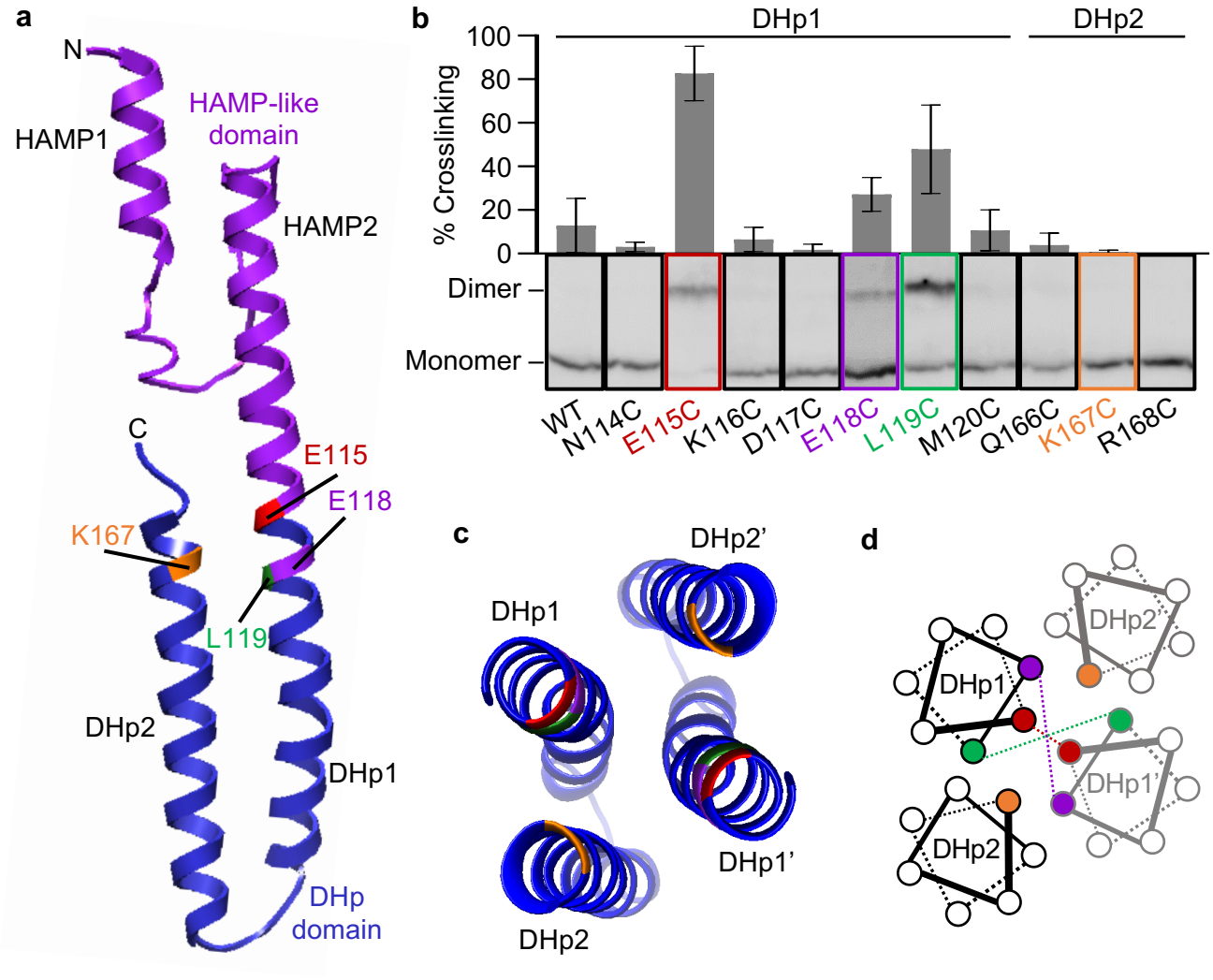

Figure 2: BceS DHp domain forms a four-helix bundle. a, Homology model of the BceS HAMP-like and DHp domains generated by I-TASSER (C-score = -0.76). The HAMP-like domain is shown in purple and the DHp domain in blue. The residues that form Cys-crosslinks in panel b are highlighted, E115 (red), E118 (purple) and L119 (green). Residue K167, which sits opposite E115, is shown in orange. **b**, Percentage of crosslinking for each BceS Cys variant was calculated from relative band intensities between monomer and dimer within each lane using Fiji (45). Amino acid substitutions were introduced in parent construct *bceS*^{WT}-His$_8$ (SGB369) and BceS production was controlled by addition of 0.02 % (w/v) xylose. Data are shown as mean ± SD from 2-5 independent repeats. **c, d**, Schematic diagram of the BceS DHp dimer configuration. Helices labelled DHp1' and DHp2' show the second protomer. Left, top down view of the helices in the structural model; right, helical wheel diagram of the top two helical turns in the DHp domain; residues that form crosslinks are highlighted as before.

134 the native copy of *bceS* and carrying a single-copy ectopic construct for expression of *bceS*
135 with a C-terminal His_8-tag, allowing slight over-production of the kinase to facilitate
136 detection by Western blot analysis. BceS contains three native Cys residues, C45 in the
137 second transmembrane helix and C198 and C259 in the ATPase domain. Based on their
138 physical distance from each other and the DHp domain, we did not expect these residues to
139 interfere with our analysis, and indeed no crosslinking product was observed upon oxidation
140 with iodine in wild-type BceS (Fig. 2b). Next, single cysteine substitutions were introduced
141 in the first two helical turns of the helix DHp1 (N114 to M120), and in equivalent positions
142 near the end of the helix DHp2 (Q166 to R168). Disulfide bond formation in these variants
143 should only occur if the substituted residues come into close proximity in the kinase dimer
144 (30). The only residues that consistently formed detectable crosslinks were at positions 115,
145 118 and 119, with the highest degree of crosslinking at position 115 (Fig. 2b). This is in good
146 agreement with their positioning at the core of the four-helix bundle and shows that the
147 structural model closely reflects the conformation of BceS in the cell (Fig. 2c).

148 To ensure that the introduction of cysteines had not affected the integrity of the protein, we
149 tested the activity of each BceS variant *in vivo*. This was based on their ability to induce
150 expression from the system's target promoter fused to a reporter gene (P_{bceA}-*luxABCDE* or
151 P_{bceA}-*lacZ*), following exposure to the antibiotic bacitracin (4). Only the K116C and K167C
152 substitutions led to a complete loss of activity (Fig. S1a). It is therefore possible that the lack
153 of crosslinking observed for the latter, which also faces the core of the DHp domain (Fig. 2c),
154 could be explained by defects in the protein rather than the distance between DHp2 helices in
155 the kinase dimer.

156 **Charge substitutions in the DHp core suggest a rotation mechanism of kinase**
157 **activation.** Closer inspection of the DHp domain revealed a striking concentration of charged

158 residues at the membrane-proximal end of the four-helix bundle (Fig. 3). In the wild-type
159 kinase, E115 and K167 create a net neutral charge in the bundle core. As described above and
160 previously (4), cells harbouring wild-type BceS strongly activate expression of the P_{bceA}-*lux*
161 reporter in the presence of bacitracin, while in the absence of the antibiotic the activity of the
162 reporter is below the detection limit (Fig. 3a, WT). Interestingly, creation of an 'all negative'
163 (K167D substitution) or 'all positive' (E115K substitution) DHp core resulted in a massive
164 increase in the basal level of the kinase, while the activity in the presence of the inducer
165 remained unaffected (Fig. 3a). To test whether this effect was indeed due to the changes in
166 core charge and not to substitutions at this position *per se*, we introduced a series of other
167 amino acids into position 115. Exchanging E115 for a different positively charged amino
168 acid, Arg, again resulted in an increase in basal activity, although less pronounced (Fig. S1c).
169 Substitution for Ala or Cys had no detectable effect on activity, showing that the presence of
170 charged amino acids was not in itself important for kinase function. Moreover, the
171 constitutive kinase activity could be returned to near wild-type levels by restoring the net
172 neutral charge through combining the E115K and K167D substitutions (Fig. 3a). We
173 therefore concluded that the high constitutive activity in the absence of the inducer was
174 indeed due to the presence of four residues with the same charge in the DHp domain core.

175 In the current model for histidine kinase activation, the DHp domain undergoes a helical
176 rotation (18). The strong activating effect we observed upon introduction of four residues of
177 the same charge at the core of the domain made it tempting to speculate that charge repulsion
178 may force BceS to undergo such a rotating motion, placing it in its activated state. According
179 to our homology model, rotation of the helix DHp1 in a counter-clockwise direction and
180 DHp2 in clockwise should create two new points of contact between charged residues: point I
181 between E118 and K167, and point II between K116 and R168 (Fig. 3b). The opposing
182 charges in point I should have a stabilizing effect on the rotated state, and removing this in

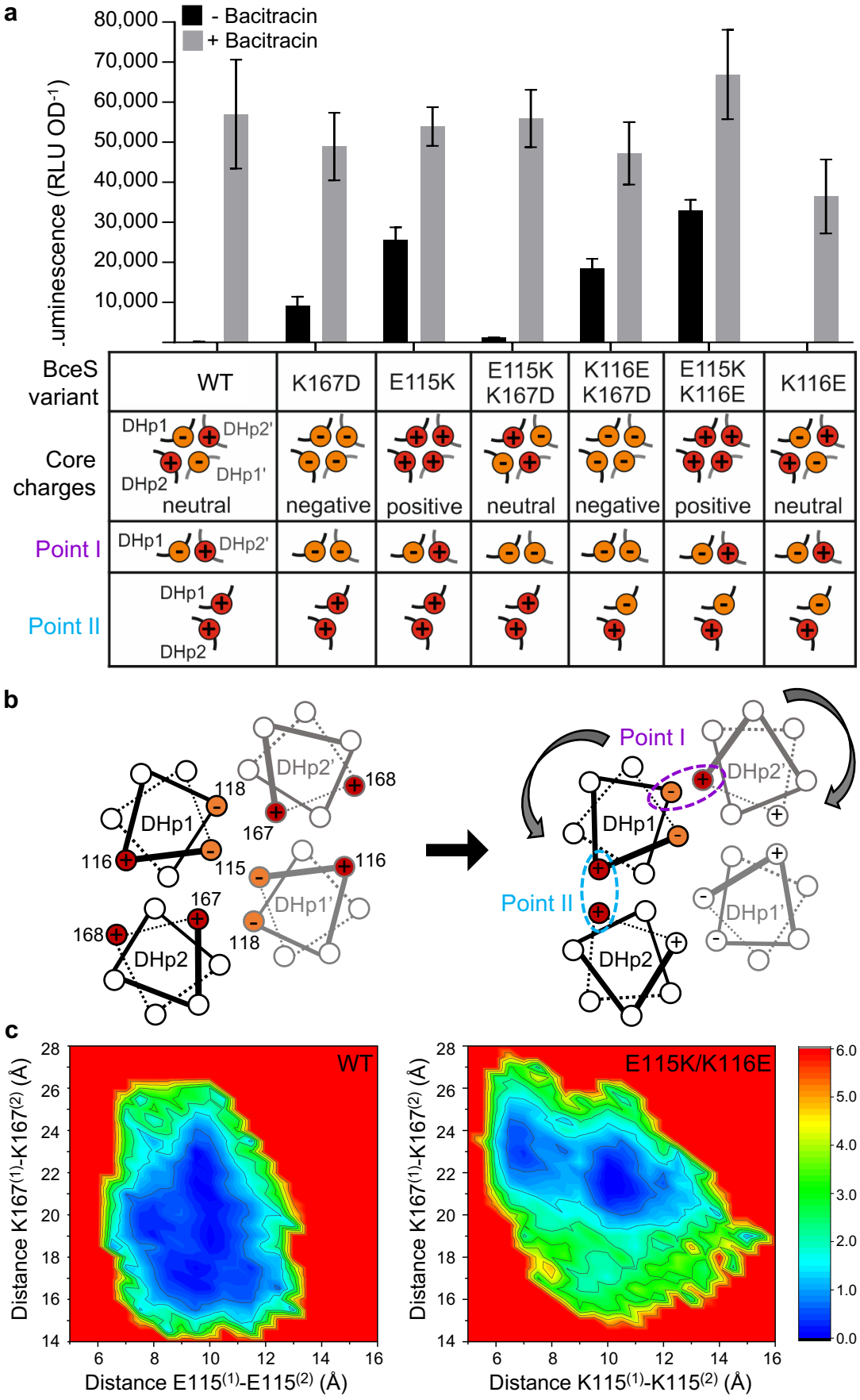

Figure 3: Charges within the BceS DHp domain core affect kinase activity. a, BceS signaling activity in strains harbouring P_{bceA}-*luxABCDE* and P_{xyl}-*bceS*. Amino acid substitutions were introduced in parent construct *bceS*^{WT}-His$_8$ (SGB369). Signaling was induced with 1µg ml^{-1} of bacitracin. Data are shown as mean ± SD from 4-22 biological repeats. The schematic below shows the location of individual and net charges in the core and stabilisation points within the four-helix bundle, as illustrated in panel b. Red, positive charge; orange, negative charge. **b**, Helical wheel diagram of the top two helical turns in the DHp dimer configuration showing location of charges and stabilisation points (pink and cyan). Helices labelled DHp1' and DHp2' show the second protomer. Black curve arrows denote the direction of helical rotation. **c**, 2D plots of potential of mean force (PMF) obtained in GaMD simulations of the wild type (WT, left) and E115K/K116E variant (right) protein. Inter-monomer distances shown are between the Cα carbon atoms of residues at positions 115 (x-axes) and 167 (y-axes). The PMFs are projected onto the surface in kcal mol^{-1} indicated by the heat scale.

183 the K167D variant may explain its lower basal activity compared to E115K (Fig. 3a). In
184 contrast, the proximity of two positive charges in point II should have a de-stabilizing effect.
185 Replacing one of these with a negative charge (K116E) by itself had no effect on kinase
186 activity. However, combining K116E with the activating effect of the E115K substitution led
187 to a further increase of basal kinase activity compared to E115K alone (Fig. 3a). This effect is
188 entirely consistent with kinase activation through helical rotations in the DHp domain, where
189 we could achieve the highest artificial activation of the protein through creating charge
190 repulsion in the kinase core, while stabilizing the rotated state through opposing charges in
191 the two new points of contact.

192 Attempts were made to detect this DHp domain rotation *in vivo* using cysteine crosslinking,
193 either following induction with bacitracin or using the constitutively active E115K/K116E
194 variant. No quantitative conclusions could be drawn, however, due to the very large
195 experimental errors (Fig. S2). To provide further evidence of conformational change in the
196 DHp domain, we turned to molecular dynamics (MD) simulations. As discussed above, the
197 homology model (Fig. 2) shows excellent agreement with experimental validation, indicating
198 that it is a reasonable starting point for MD simulations. Given the relatively large putative
199 rotation, we applied Gaussian accelerated MD (GaMD) to more completely sample
200 conformational space. This approach applies a harmonic boost potential to effectively
201 'flatten' the free energy landscape, thereby enhancing the conformational sampling achieved
202 during MD simulation (31).

203 To assess conformational differences in the DHp domain between the wild-type kinase and
204 the constitutively active E115K/K116E variant, GaMD simulations were performed on both
205 for a total of 2 µs each (four replicas of 500 ns; Figure S3a). From our simulations, we
206 calculated the potential of mean force (PMF) for a series of internuclear distances for both

207 wild-type and variant residues. These values can serve as a proxy for the energetic barrier
208 between conformational sub-states. To best illustrate the relative orientation of helices in the
209 DHp domain bundle, we focused on positions 115 and 167, facing the bundle core (Fig. 3).
210 The PMF plots for the internuclear pairs of these residues between monomeric units of the
211 DHp domain are shown in Figure 3c. The lower the PMF value, the more likely the helices
212 will occupy the conformational state defined by the internuclear distances shown. In the wild-
213 type DHp domain, the PMF plot for distances between monomers at amino acids 115 and 167
214 shows a broad minimum across most of conformational space (Fig. 3c, left). This suggest that
215 there is a relatively high propensity for the domain to explore a diversity of conformational
216 space. Figure 3c (right) shows the same data for the variant DHp. Instead of the broad
217 minimum that characterizes the wild-type domain, the variant now shows two distinct, more
218 restricted minima. More specifically, the tendency towards a longer K167 distance in the
219 variant DHp would seem consistent with our model for helix rotation (Figure 3b). To more
220 clearly explore the differences between conformational space accessed by the wild-type and
221 variant DHp domain, we performed principal components analysis (PCA) of the data from
222 Figure 3c. This indicates that there is a significant difference in the principal component
223 space sampled by the wild-type and variant DHp (Fig. S3b). That is, the variant DHp
224 occupies a conformational space that is not accessible to the wild-type domain. Based on the
225 high constitutive activity of the variant, it is plausible to assume that this new conformational
226 space represents the active state of the kinase. Importantly, our simulations show that the
227 wild-type kinase is unable to adopt this conformation on the simulated time scales. This is
228 consistent with our *in vivo* experimental data that shows no detectable kinase activity without
229 activation through the sensory transporter BceAB.

230 **BceS contains a HAMP-like signal transfer domain.** Contrary to previous predictions, the
231 BceS homology model showed a domain with structural similarity to a HAMP domain

232 between the second transmembrane helix and the DHp domain. HAMP domains adopt a
233 parallel four-helix bundle arrangement with two alternative states of helix packing that
234 transmit a conformational change from an upstream input to a downstream output domain
235 (18, 32, 33). While there is some argument over the exact motions within HAMP domains,
236 there seems to be agreement that they turn multiple input movements consistently into a
237 helical rotation (18, 33). The four-helix bundle is stabilized through multiple packing layers,
238 forming both inter- and intramolecular interactions, predominantly mediated by hydrophobic
239 residues (33, 34). A protein sequence alignment of known HAMP domains and the HAMP-
240 like domain of BceS is shown in Fig. 4a, with the positions of the critical packing points
241 highlighted. The hydrophobicity at these positions is largely conserved in BceS, with the
242 exception of two positions occupied by negatively charged Glu instead. Additionally, the Pro
243 residue at the N-terminus of helix 1, and Glu at the N-terminus of helix 2, which are
244 conserved in HAMP domains, are not present in BceS (Fig. 4a). Due to these key differences
245 to the canonical domain, we decided to refer to this domain as 'HAMP-like'.

246 Previous investigations of HAMP domains have highlighted one particular residue with key
247 influence on the signaling state. This residue corresponds to L67 in BceS, a position most
248 commonly occupied by small hydrophobic residues that favour bundle packing (A or V,
249 occasionally I, L; Fig. 4a, black arrow) (33). Based on extensive structural work on the
250 HAMP domain of the *A. fulgidus* protein Af1503, this residue (A291 in Af1503) has a crucial
251 role in controlling the conformational state of the HAMP domain. Specifically, it is thought
252 that increasing residue size at this position decreases the threshold for conversion between
253 packing states of the HAMP domain and can cause increased signal responsiveness or
254 elevated kinase activity, while smaller residues decrease activity (33, 35, 36)·(37).

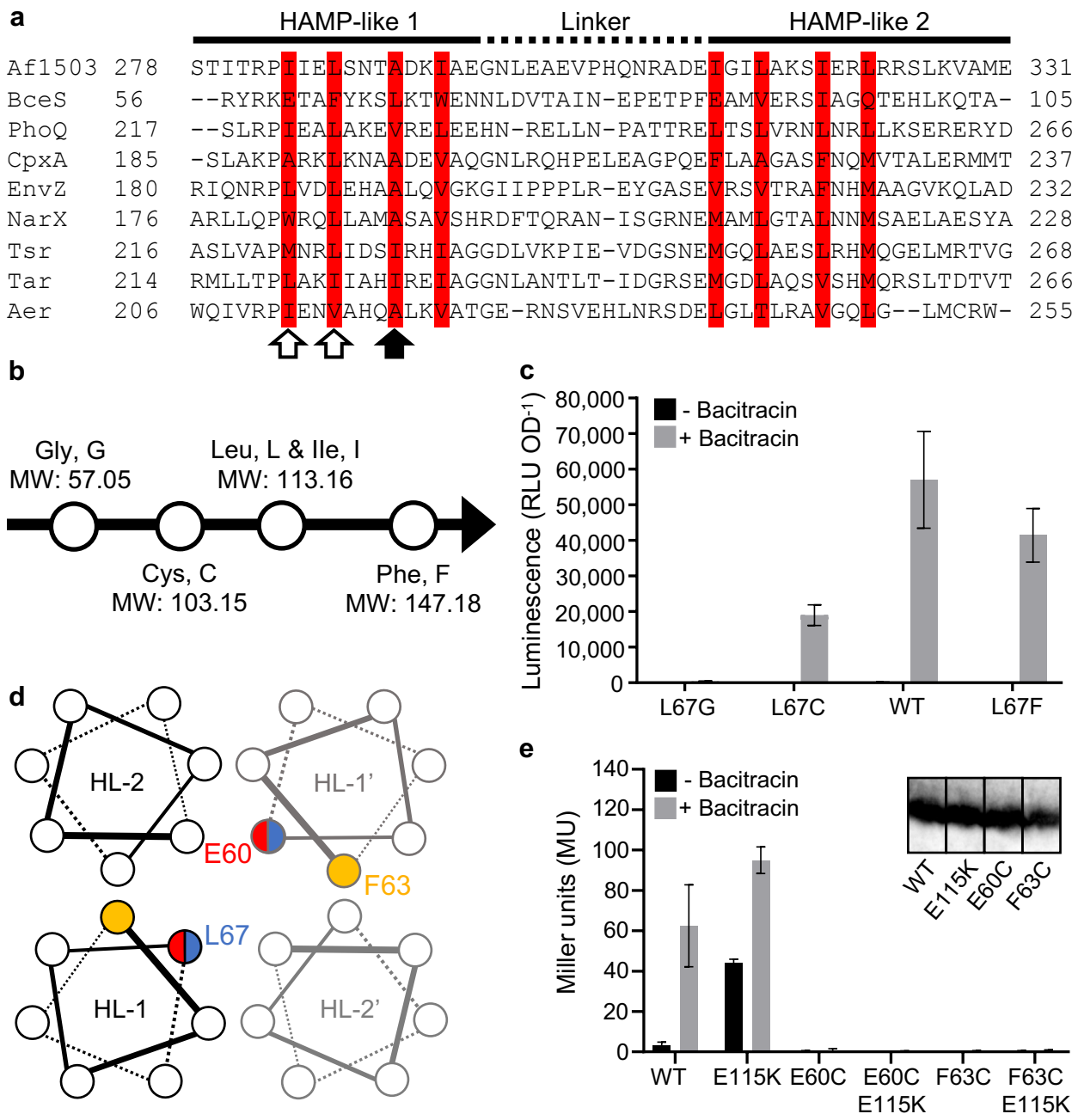

Figure 4: BceS contains a HAMP-like signal transfer domain. a, Sequence alignment of known HAMP domains and the BceS HAMP-like domain generated with ClustalO. Residues in red form the packing layers in the Af1503 HAMP domain. The black solid arrow indicates the packing residue that influences signaling state in some HAMP domains. White open arrows indicate E60 and F63 critical for BceS function. Proteins included and their GenBank identifiers are Af1503 (O28769), BceS (BSU30390), PhoQ (P23837), CpxA (P0AE82), EnvZ (P0AEJ4), NarX (P0AFA2), Tsr (P02942), Tar (P07017), Aer (P50466). **b**, Schematic showing amino acids and their sizes in MW used in size substitutions. **c**, BceS signaling activity following L67 amino acid size substitution harbouring P_{bceA}-*luxABCDE* and P_{xyl}-*bceS*. Amino acid substitutions were introduced in the parent construct *bceS*^{WT}-His_8 (SGB369). Signaling was induced with 1µg ml^{-1} of bacitracin. Data are shown as mean ± SD from 5-18 biological repeats. **d**, Helical wheel diagram of the HAMP-like domain. Individual helices are abbreviated HL-1 and HL-2; the labels HL-1' and HL-2' show the second protomer. Residues essential for BceS activity are E60 (red) and F63 (yellow); the key packing residue L67 is shown in blue; red/blue semicircles are used to indicate positioning of residues in subsequent helical layers. **e**, BceS signaling activity of the constitutive ON variant (BceS^{E115K}) combined with loss-of-function substitutions at positions 60 and 63. Amino acid substitutions were introduced in parent construct *bceS*^{WT}-His_8 (SGB401). Signaling in cells harbouring P_{bceA}-*lacZ* and P_{xyl}-*bceS* was induced with 1µg ml^{-1} of bacitracin, BceS production was controlled by addition of 0.02 % (w/v) xylose. Data are shown as mean ± SD from 3-7 biological repeats. The inset shows an anti-His Western blot analysis to confirm membrane localisation and protein levels of wild-type (WT) BceS and its variants.

255 To test if the HAMP-like domain discovered in BceS fulfils an equivalent function to *bona*
256 *fide* HAMP domains, we therefore investigated the role of amino acid size at this position by
257 changing L67 to the smaller Gly and Cys, as well as the larger Phe side chain (Fig. 4b).
258 Indeed, smaller size substitutions reduced BceS activity, up to a near-complete loss of
259 induction in the Gly variant (Fig. 4c). Increasing the size to Phe, however, did not lead to an
260 increase of signaling nor a change in basal activity of BceS. Our data are thus consistent with
261 the notion that small residues at this position may increase the threshold for conversion
262 between HAMP-domain conformations (33, 35), but we could not find a stimulating effect
263 through a larger residue. The precise effect of changing this residue may therefore depend on
264 the specific context in different proteins. We nevertheless conclude from our data that the
265 HAMP-like domain in BceS is likely to be a functional equivalent to conventional HAMP
266 domains in other proteins and thus contributes to signal transfer within the histidine kinase.

267 For further functional investigation, we carried out Cys scanning mutagenesis of both helices
268 within the HAMP-like domain. The majority of variants maintained at least partial signaling
269 activity (Fig. S4), and in contrast to other studies (37, 38), we did not find any substitutions
270 that led to a constitutively active state of BceS. The only two substitutions that caused a
271 complete loss of function were E60C and F63C (Fig. 4 and S4). Interestingly, these fall on
272 the first two positions of the packing motif (Fig. 4a, white arrows and 4d), with E60 located
273 one packing layer above the critical L67 discussed earlier, and are therefore likely of
274 structural importance. Both variant proteins are present in the cytoplasmic membrane at the
275 same levels as the wild type protein according to Western blot analysis (Fig. 4e inset),
276 showing that the lack of signaling is not caused by general protein misfolding. To test if the
277 defect of the two variants was due to a loss of signal transfer from either the TM region of the
278 protein or the transporter, we combined each of the LOF mutations with the E115K
279 substitution that activates BceS in the absence of a stimulus. All resulting variants remained

280 completely inactive (Fig. 4e), which showed that the substitutions in the HAMP-like domain
281 had a dominant effect and thus likely caused substantial structural disruptions in the protein,
282 rather than specifically affecting signal transfer.

283 **Activation of BceS involves a piston-like displacement in transmembrane helix 2.** We
284 next investigated the conformation of the second transmembrane helix in BceS. In many
285 histidine kinases, conformational changes in an extracellular sensory domain are transmitted
286 to the cytoplasmic region through physical movement of the intervening transmembrane helix
287 (17). In the case of BceS, however, signaling is entirely reliant on the BceAB transport
288 system and therefore does not involve canonical transmembrane information transfer. To
289 investigate if BceS activation nevertheless involved transmembrane helix movements, we
290 carried out a cysteine accessibility scan (Scan-SCAM, (21)) of its second transmembrane
291 helix. This analysis requires a cysteine-free background, and we therefore replaced the three
292 native Cys residues mentioned earlier by serine and confirmed that he C45S/C198S/C259S
293 BceS variant was still fully functional (Fig. S5). Individual cysteine replacements were done
294 from positions 51 to 65, surrounding the predicted membrane interface at W54 or F55. The
295 essential residues E60 and F63 were not replaced. All variants were signaling competent (Fig.
296 S5). The position relative to the membrane was then tested for each Cys residue based on its
297 solvent accessibility, using a modified version of the established *E. coli* protocol (21). In
298 brief, treatment of whole cells with N-ethyl-maleimide (NEM) should block any solvent-
299 exposed Cys residue, whereas in untreated cells the sulfhydryl groups should remain
300 available for later reactions. Following isolation of membranes, any unblocked Cys residues
301 are then reacted with methoxypolyethylene glycol maleimide (PEG-mal), resulting in a 10
302 kDa increase in size, detectable by Western Blotting. For cytoplasmic Cys residues in BceS,
303 we therefore expected to see a shift in size only in samples that had not been treated with
304 NEM (Fig. 5, blue labels). In contrast to the established *E. coli* methodology (21), we could

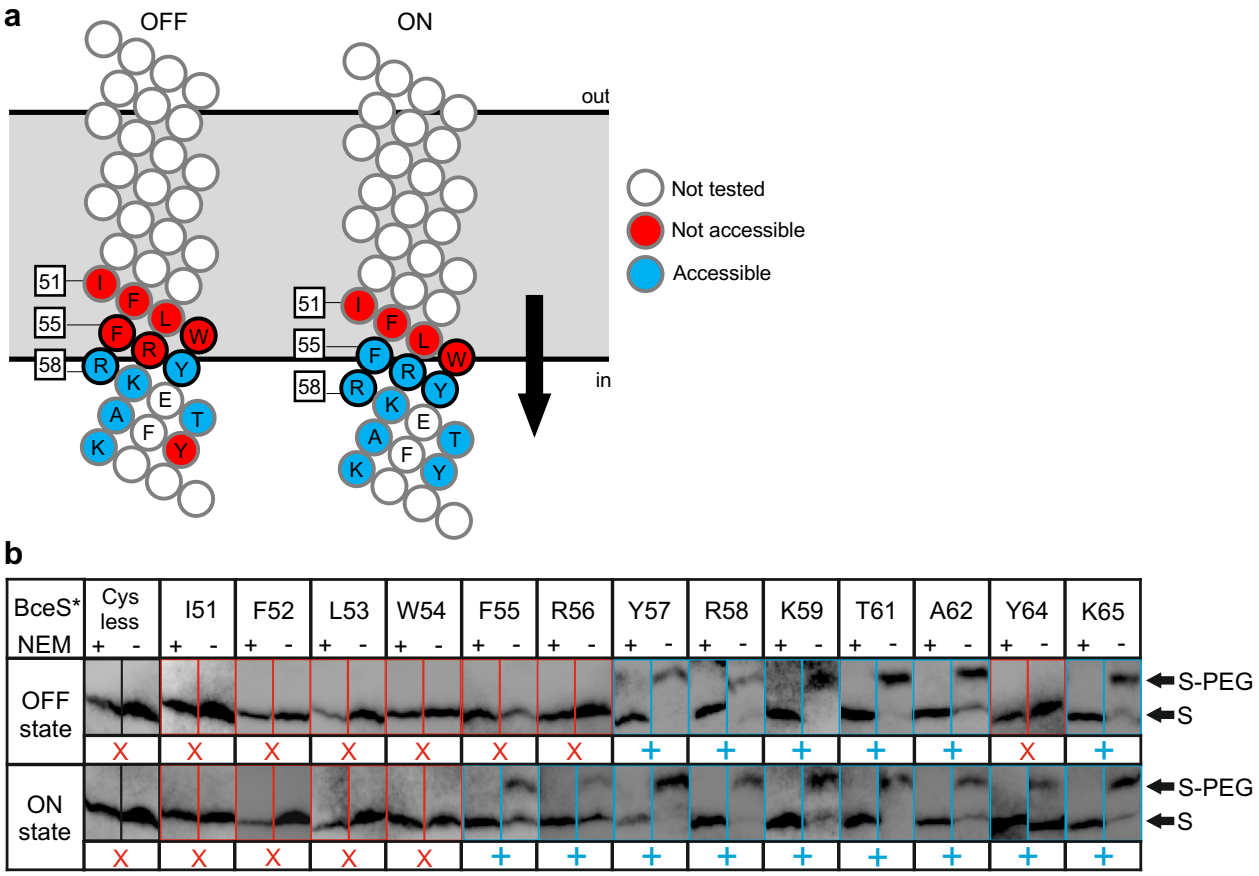

Figure 5: Accessibility of Cys residues at the membrane interface shows a piston-like displacement upon BceS activation. a, Schematic representation of transmembrane helix 2 in the OFF and ON states, respectively. Relevant native amino acids are indicated in one-letter code. Solvent-accessible (PEGylated) Cys replacements are shown in blue, inaccessible (unPEGylated) Cys replacements in red and residues not tested in white. Residues circled in black were tested in triplicate, those circled in grey in duplicate. **b**, Anti-His Western blot analysis of solvent-accessibility of Cys replacements (Scan-SCAM). Bands corresponding to PEGylated (S-PEG) and unmodified (S) BceS are indicated; individual lanes are outlined in the same colour code as used in panel a. 'Cys-less' indicates the parent variant of BceS lacking its native Cys residues. OFF state: amino acids substituted in parent construct *bceS*$^{C45S/C198S/C259S}$-His$_8$ (SGB936). ON state: amino acids substituted in parent construct *bceS*$^{E115K/K116E/C45S/C198S/C259S}$-His$_8$ (SGB951).

305 not observe PEGylation of membrane-embedded Cys residues in *B. subtilis*, regardless of the
306 presence of SDS, possibly due to differences in membrane composition. We therefore
307 interpreted those residues as being membrane embedded that did not show a size shift in
308 either presence or absence of NEM treatment (Fig. 5, red labels). Our results showed that
309 residues up to position 56 resided in the solvent-inaccessible membrane environment, while
310 residues from Y57 onwards were accessible and therefore cytoplasmic (Fig. 5, 'OFF state').
311 It is not clear why residue Y64 was consistently mapped as inaccessible, however, given its
312 distance from the likely membrane interface this was considered an artifact and not further
313 interpreted. We then repeated the same analysis in the background of the E115K/K116E
314 substitutions that place the kinase in a constitutively active conformation. Here, residues from
315 F55 onwards became consistently solvent-accessible (Fig. 5, 'ON state'). Comparison of the
316 two states therefore shows that BceS activation involved an inward piston-like displacement
317 by two amino acids of the second transmembrane helix.

318 We next sought to test whether BceS could be activated by artificially inducing a shift
319 through introduction of positively charged arginine residues near the membrane interface.
320 This approach has been shown to cause signal-independent activation of the *E. coli* histidine
321 kinase DcuS (21). We therefore substituted three of the residues near the cytoplasmic end of
322 transmembrane helix 2 of BceS (W54, F55 and Y57) with Arg, individually and in pairs.
323 (Fig. S6). Variants containing the W54R substitution had approximately 60% higher
324 activities upon stimulation with bacitracin (Fig. S6), which may indicate a stabilisation of or
325 lowered transition threshold to the activated state. However, none of the variants showed a
326 detectable change of basal activity in the presence or absence of the input transporter BceAB,
327 leading us to conclude that Arg substitution alone was not sufficient to activate the kinase,
328 which still relied on BceAB for signaling.

329 **The transporter BceAB has complete control over kinase conformation**. It was
330 previously shown for Bce of *B. subtilis* and several other examples of the same type of
331 resistance system that activation of signaling is completely reliant on the ABC transporter (6,
332 7, 10, 11, 27). We further showed through computational modelling that the signaling output
333 via BceS is directly proportional to the activity of BceAB and does not follow the switch-like
334 on/off behaviour seen in most other systems using transporters as accessory sensing proteins
335 (4, 23). This led us to hypothesise that BceAB completely controls the conformation of BceS
336 within the sensory complex and thus slaves kinase activity directly to its own transport
337 activity. Our discovery of the DHp domain variants that cause artificial activation of BceS
338 now for the first time enabled us to test this hypothesis experimentally by investigating the
339 role of BceAB in controlling the OFF state of the kinase.

340 In cells harbouring the wild-type sequence of BceS, the OFF-state activity in un-stimulated
341 cells was below the detection limit of our assays, and deletion of the transporter therefore has
342 no measurable effect (Fig. 6a). However, in the E115K or the E115K/K116E variants, basal
343 kinase activity was high, allowing us to test the effect of *bceAB* deletion in the absence of
344 bacitracin. Removing the transporter in this background caused a striking further increase in
345 activity, rendering the kinase fully activated irrespective of the presence of the inducing
346 antibiotic (Fig. 6a). Therefore, in the absence of its substrate, the inactive transporter can
347 inhibit the activity of the constitutively active DHp domain variants, which manifests as an
348 approximately ten-fold reduction in basal activity compared to the transporter-free state. Our
349 data are consistent with a model where inactive BceAB exerts close control over BceS
350 keeping the kinase in its inactive state (Fig. 1, left). This reveals a further layer of kinase
351 control in addition to the transporter's known activating effect (4), and would prevent any
352 spurious signaling in the absence of antibiotics.

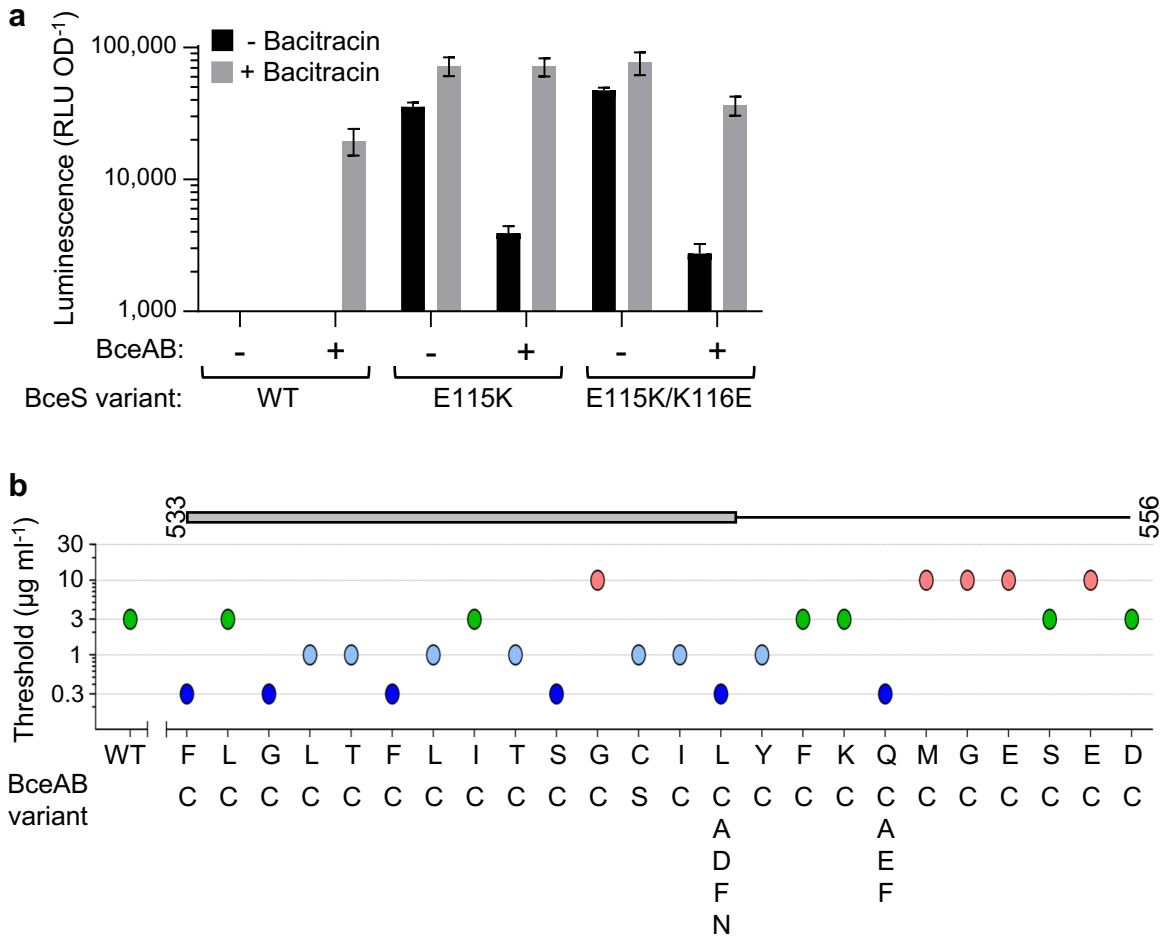

Figure 6: Control of BceS activity by the transporter BceAB. a, Signaling activity of BceS measured in strains harbouring P_{bceA}-*luxABCDE* and challenged with 10µg ml^{-1} of bacitracin (grey) or left untreated (black). Amino acid substitutions were introduced into parent construct P_{xyl}-*bceS*-His_8, in a strain background carrying a Δ*bceS* deletion (BceAB +; SGB792), or a Δ*bceSAB* deletion (BceAB -; SGB818). Data are shown as mean ± SD from 5-12 biological repeats. **b,** Signaling phenotype of BceAB variants. Amino acid substitutions were introduced into the P_{xyl}-*bceAB*-$FLAG_3$ parent construct, and signaling assessed using either a P_{bceA}-*lacZ* (SGB370 and derivatives) or P_{bceA}-*luxABCDE* (SGB731 and derivatives) reporter. Cells were challenged with a series of bacitracin concentrations, and the lowest concentration giving signaling above background is shown by circles in the plot (see Fig. S7 for complete datasets). Analyses were based on mean values from at least three independent repeats. The first line of x-axis labels gives native amino acids, the lines below indicate substitutions tested. The bar above the graph shows positions in the BceB sequence and areas within the membrane (grey bar) or in the cytoplasm (black line). Circle colours are assigned green, wild-type (WT) signaling threshold; red, increased signaling threshold; blue, reduced signaling threshold.

353 **BceAB has not evolved for maximal signaling sensitivity.** Recent structural work has
354 provided new insights into the functional mechanism of the Type VII superfamily of ABC
355 transporters, of which BceAB is a member. This group of proteins is thought to act as
356 mechanotransmitters, using cytoplasmic ATP hydrolysis to provide energy for periplasmic
357 processes, such as removal of antibiotics (39). In *E. coli* MacB, mechanotransmission is
358 achieved by the transmembrane helix linking the cytoplasmic ATPase interaction site to the
359 periplasmic domain (39). In BceAB, the equivalent region is its eighth transmembrane helix,
360 which connects the transporter's extracellular domain to a cytoplasmic loop containing one of
361 the ATPase contact interfaces (Fig. 1, dark green) (15). Based on our earlier discovery that
362 this region of BceB contained a particularly high density of mutations leading to a loss of
363 signaling (40), we speculated that this region was crucial for the communication between
364 transporter and kinase. We therefore carried out another Cys scan, individually replacing
365 each residue from positions 533 to 556 in BceB, encompassing approximately half of
366 transmembrane helix 8 and the first alpha-helical segment of the adjacent cytoplasmic region.
367 The native Cys at position 544 was replaced by Ser. Expression of *bceAB* was from a xylose-
368 inducible promoter to ensure consistent transporter production irrespective of signaling
369 activity. The resulting variants, except G535C, displayed comparable bacitracin resistance to
370 the isogenic progenitor strain (Table S4), confirming full functionality of the transporters.
371 When signaling was tested using our standard reporter gene assays, all variants except
372 G543C reached a similar amplitude of reporter induction as strains containing the wild-type
373 construct (Fig. S7 a&b). However, we observed some clear difference in the sensitivity of
374 signaling, i.e. the minimal concentration of antibiotic required to elicit a response. In cells
375 with the wild-type construct, the lowest bacitracin concentration to trigger signaling was 3 µg
376 ml^{-1}, while a number of variants had a higher threshold of 10 µg ml^{-1} (Fig. 6b, green vs red
377 dots; Fig. S7 a&b). The majority of these fell into the C-terminal part of the scanned region,

378 indicating potential defects in coupling to the ATPase. To our surprise, we also found several
379 variants that showed a marked increase in signaling sensitivity and responded already at 0.3
380 μg ml^{-1} or even 0.03 μg ml^{-1} bacitracin (Fig. 6b, dark blue dots; Fig. S7). We had previously
381 seen that a reduction of BceAB transport activity can cause such a shift in signaling
382 threshold, because the negative feedback created by removal of the antibiotic is missing (4).
383 However, as none of these variants showed any change in bacitracin resistance (Table S4),
384 loss of antibiotic removal cannot explain the increased signaling sensitivity. Mapping of these
385 residues showed that they occurred with a regular periodicity of every four amino acids (Fig.
386 6b), suggesting they are positioned along the same face of the transmembrane helix. Figure
387 S7c shows a homology model from I-TASSER of the final three transmembrane helices of
388 BceB, for which MacB was the closest structural analog, to illustrate the potential
389 arrangement of these residues. Substitutions with the relatively small amino acid Cys may
390 have enabled tighter helix packing, potentially contributing to more effective signaling. To
391 test this, we replaced two of the positions, L546 and Q550, with a series of other amino acids,
392 including small Ala; charged Glu or Asp; and large Phe. Regardless of the substitution made,
393 deviation from the wild-type sequence at these positions consistently led to an increase in
394 signaling sensitivity (Fig. 6b). It is difficult to envisage that all these substitutions caused
395 tighter interactions with the kinase. An alternative explanation may be that they are involved
396 in tightly coupling ligand binding by the extracellular domain to ATP hydrolysis, and that
397 substitutions weaken this coupling, allowing ATP hydrolysis and therefore signaling to occur
398 at lower substrate concentrations. Despite numerous genetic and biochemical attempts, the
399 precise residues with which BceS and BceB interact remain unknown, and we believe this is
400 likely due to an extensive interface between the proteins involving multiple contacts. While it
401 was beyond the scope of this study to pursue a further functional characterization of the
402 transporter, our findings clearly show that BceB contains a series of residues that likely form

403 a continuous face on transmembrane helix 8, which prevent signaling from occurring at lower
404 bacitracin concentrations. Given that any replacement we tested led to more sensitive
405 signaling, we therefore conclude that the transporter has evolved to avoid such hyper-
406 sensitive signaling, constituting a further layer in minimizing the fitness cost of resistance.
407 Under laboratory conditions, we have so far not been able to detect a competitive
408 disadvantage in strains that harboured hyper-sensitive variants of BceAB. However, fast
409 growth in carefully controlled conditions is not representative of the complex microbial
410 interactions in natural habitats, where energy-conserving regulatory strategies will likely
411 contribute to the competitive success of a microorganism.

412 **DISCUSSION**

413 In this study, we set out to investigate the molecular mechanisms of the flux-sensing strategy
414 employed by Bce-like antibiotic resistance systems. Their hallmark feature is that histidine
415 kinase activity not only fully depends on the presence of its cognate transporter, but is
416 directly proportional to transport activity across a large input dynamic range of antibiotic
417 concentrations (4). This careful adaptation of signaling activity ensures the resistance
418 transporter is produced precisely to the cell's demand for detoxification capacity, a very cost-
419 efficient strategy to control gene expression. The results presented here now provide
420 molecular level understanding of how such close control over kinase activity can be
421 achieved.

422 Analyses of BceS conformation in the inactive and active state showed a piston-like inward
423 displacement of the second transmembrane helix and helical rotation within the DHp domain
424 upon kinase activation. Tertiary structure predictions and experimental validation indicate
425 that BceS possesses an intervening HAMP-like domain that likely fulfils a signal transfer
426 function. Based on crystallographic evidence from a truncated kinase, it has been proposed

427 that in HAMP-containing histidine kinases ligand binding typically induces piston-
428 displacements in the membrane, and these are converted by the HAMP domain into rotational
429 motion of the DHp domain (18). Despite its unusual input mechanism via the BceAB
430 transporter, the conformational changes we observed within BceS are therefore consistent
431 with this proposed mode of activation.

432 A recent NMR study reported on the structure of the BceS-like kinase NsaS from *S. aureus*,
433 which possesses a much shorter linker region between its transmembrane and DHp domains.
434 This linker region adopts a coiled-coil conformation instead of the HAMP-like fold of BceS
435 (20). Inspection of kinase sequences in an existing collection of Bce-like resistance systems
436 (8) showed that the vast majority of these proteins contained the larger version of the linker
437 (approximately 60 amino acids), and only a small number possessed short (around 20 amino
438 acid) linkers with a predicted coiled-coil motif. BceS therefore appears to be the more typical
439 subtype of this group of kinases than NsaS. Interestingly however, akin to the alternative
440 helix packing mechanism proposed for HAMP domains (33), activation of NsaS was also
441 proposed to involve switching between helical packing states of the coiled-coil (20). The
442 molecular principles of activation may therefore be conserved between both subtypes of
443 BceS-like kinases.

444 To further investigate the activation mechanism of BceS, we sought to force each of the
445 conformational changes via amino acid substitutions. Charge repulsion at the core of the DHp
446 domain to trigger helical rotation consistently led to kinase activation without a physiological
447 stimulus (Fig. 3). However, we were unable to artificially trigger activation through
448 substitutions that should have induced piston displacements in the membrane (Fig. S6) or
449 induced the active conformation of the HAMP domain (Fig. 4 and S4). This is in contrast to
450 studies of other kinases where such substitutions least partially raises the basal activity (21,

451 37, 38). In canonical histidine kinases, the input signal is detected directly, e.g. through
452 ligand binding. One could therefore speculate that in these proteins, conformational changes
453 have to be smoothly transmitted from each domain to the next, and that this is reflected in the
454 relative ease with which kinase activity can be artificially induced through changes in each
455 individual domain. In contrast, BceS-like proteins are subject to control by the transporter.
456 While we do not yet know with which part of the kinase the transporter interacts, it is
457 conceivable that in a kinase that relies on such external control, small changes in upstream
458 domains are insufficient to trigger rotation of the DHp domain, and only genetic
459 manipulation of the domain itself can cause artificial activation. Some support for such a
460 hypothesis may be found in the MD simulations, which showed that the wild-type DHp
461 domain does not by itself sample the conformational space observed in the active variant
462 (Fig. S3), implying that the transporter is likely required to provide the necessary force for
463 transition to the active state.

464 The use of transporters in accessory control of signaling proteins is not uncommon in
465 bacteria, but BceAB is unusual in that it is an activator of signaling, while most other
466 transporters act as repressors (23). Repression of signaling and its relief are easily envisaged
467 via formation and dissociation of a repressive complex between transporter and histidine
468 kinase. For the Bce system, we previously showed that transporter and kinase constitutively
469 form a signaling complex in the membrane, irrespective of the presence or absence of the
470 inducer, bacitracin (5). Considering its activating role and that signaling is proportional to
471 transport activity, the transporter must therefore be able to directly influence kinase activity
472 within this complex. When this was first tested *in vitro*, it was noted that BceAB had a
473 negative effect on the kinase autophosphorylation rate in the OFF state, although we could
474 not explain the observation at the time (5). In the present study, we now show that the
475 transporter indeed not only controls the ON but also the OFF state of BceS *in vivo* and is able

476 to restore partial control over the high constitutive activity of the DHp domain variant (Fig.
477 6a). We propose that through controlling both states of the kinase, the transporter is able to
478 exert the level of close control that is needed to explain the enormous dynamic range of the
479 system, where signaling is maintained in proportion to transport activity over more than three
480 orders of magnitude in antibiotic concentrations (4). A crucial feature of the flux-sensing
481 mechanism is that signaling is immediately reduced if transport activity is low, either because
482 the antibiotic threat is over or because the cell has reached sufficient detoxification capacity
483 (4). Importantly, the ability of BceAB to actively switch off BceS activity described here
484 explains how this energy-conserving signaling strategy is realized on the molecular level.
485 Control over the OFF state also allows the transporter to actively prevent any spurious
486 signaling by the two-component system in the absence of the antibiotic. Finally, our
487 mutagenesis analysis of BceAB revealed that the transporter itself has evolved to avoid
488 signaling at very low antibiotic concentrations, highlighting yet another level of cost
489 reduction.

490 Taken together, we here present a molecular level model for activation of antibiotic
491 resistance based directly on the cell's need for protection, using a flux-sensing signaling
492 strategy that employs multiple layers of active energy conservation to minimize any fitness
493 costs of resistance. The system studied here is centered on two-component signaling, one of
494 the most important regulatory features of bacteria. Our findings should therefore have wide
495 relevance and serve as a model for understanding, in general, how analog dials can control
496 fine-tuned gene expression in bacteria to achieve an optimal cost-benefit balance.

497 **EXPERIMENTAL PROCEDURES**

498 **Bacterial strains and growth conditions.** All strains used in this study are listed in table S1
499 and were routinely grown in Lysogeny Broth (LB; 10 g l^{-1} tryptone, 5 g l^{-1} yeast extract, 5 g l^{-}

500 ^{1} NaCl) at 37 ºC with aeration. Solid media contained 15 g l^{-1} agar. Selective media contained
501 chloramphenicol (5 µg ml^{-1}), macrolide-lincosamide-streptogramin B (erythromycin; 1 µg
502 ml^{-1}, lincomycin; 25 µg ml^{-1}), spectinomycin (100 µg ml^{-1}), kanamycin (10 µg ml^{-1}), or
503 ampicillin (100 µg ml^{-1}).

504 **DNA manipulation and strain construction.** All primers and plasmids used in this study
505 are given in tables S2 and S3, respectively, with the use of each primer specified in table S3.
506 Site-directed mutagenesis was carried out according to the manufacturer's instructions for the
507 QuikChange II site-directed mutagenesis kit (Agilent Technologies), or by PCR-overlap
508 extension (41). *Bacillus subtilis* transformations were carried out via natural competence as
509 previously described (42). DNA for transformation was either provided as linearised plasmid
510 DNA, or as genomic DNA from a *B. subtilis* strain already carrying the desired genetic
511 construct.

512 To allow manipulation of both *bceS* and *bceAB* sequences, an unmarked deletion strain
513 lacking all three genes (Δ*bceSAB*, SGB377) was constructed as described previously (43),
514 employing plasmid pAK102. Strains lacking *bceS* only (Δ*bceS*; TMB1036) or *bceAB* only
515 (*bceAB*::kan; TMB035 (27)) were available from previous work. Signaling activity was
516 assessed in strains harbouring a chromosomally integrated transcriptional reporter construct
517 of the target promoter P_{bceA}, fused to either *luxABCDE* (pSDlux101 (40)) or *lacZ* (pER603
518 (27)). Details of the assays used are given below.

519 Genetic manipulation of *bceS* was performed using previously constructed plasmids as
520 template. For Western blot detection, the construct pSD2E01 encoding BceS with a C-
521 terminal octa-histidine tag (P_{xyl}-*bceS*^{WT}-His_8 (5)) was employed. Un-tagged constructs were
522 derived from pAS719 (P_{xyl}-*bceS*^{WT}). Genetic manipulation of *bceAB* was performed using the
523 previously constructed plasmid pFK727, encoding BceAB with a C-terminal triple FLAG-tag

524 on the permease (P_{xyl}-*bceAB*-FLAG$_3$ (40)). All constructs used in this study integrate stably
525 and as a single copy into the *B. subtilis* W168 chromosome.

526 **Signaling activity assays.** In strains carrying the P_{bceA}-*lacZ* reporter, signaling was assessed
527 following challenge of exponentially growing cells with Zn^{2+}-bacitracin (bacitracin) and
528 measured as β-galactosidase activity (expressed in Miller Units), as described previously
529 (27). For strains carrying the P_{bceA}-*luxABCDE* reporter, luciferase activities were assayed
530 using a Tecan® Spark® microplate reader controlled by SparkControl™ V2.1 software.
531 Starter cultures were grown at 37 ºC in 2 ml of LB medium overnight, then diluted 1:1000
532 into fresh medium before adding 100 µl into 96-well plates (black, clear flat bottoms;
533 Corning®). Samples were grown at 37 ˚C with orbital agitation at 180 rpm and allowed to
534 achieve early exponential growth (OD_{600} 0.3 – 0.4), before adding Zn^{2+}-bacitracin to a final
535 concentration of 1 µg ml^{-1} unless otherwise indicated. OD_{600} and relative luminescence units
536 (RLU; integration time 1 s) were measured every 5 min and were background-corrected using
537 values from LB-only wells. RLU was normalised for cell density (RLU OD^{-1}). The reported
538 values are steady-state activities achieved 60-75 min after bacitracin addition.

539 Cells were grown without the addition of xylose, as the basal activity of the promoter P_{xylA}
540 (44), used to drive expression of the ectopic copies of *bceS* and/or *bceAB*, was sufficient to
541 achieve full signaling activity. In strains containing the native copy of *bceAB* (Δ*bceS*
542 background) signaling was induced with 10 µg ml^{-1} of Zn^{2+}-bacitracin. In strains containing
543 only the ectopic construct for BceAB production (Δ*bceSAB* background), signaling was
544 induced with 1 µg ml^{-1} of Zn^{2+}-bacitracin. These concentrations were established in our
545 earlier work as eliciting maximum signaling activity in the respective genetic backgrounds
546 (4).

547 **Bacitracin sensitivity assays.** The sensitivity of *B. subtilis* strains to bacitracin was
548 determined as described (40), with minor modifications. Serial two-fold dilutions of Zn^{2+}-
549 bacitracin from 32 µg ml^{-1} to 0.5 µg ml^{-1} were prepared in Mueller-Hinton medium
550 containing 0.2 % (w/v) xylose to ensure maximal production of BceAB. For each
551 concentration, 100 µl volumes in 96-well plates were inoculated 1:400 from overnight
552 cultures grown in Mueller-Hinton medium with xylose and selective antibiotics. Each culture
553 was scored for growth after 20 to 24 h of incubation at 37°C with aeration. The MIC was
554 determined as the lowest bacitracin concentration where no visible growth was detected.

555 **Cysteine cross-linking *in vivo*.** Cysteine cross-linking was assessed in strains carrying the
556 Δ*bceSAB* deletion complemented with xylose-inducible ectopic copies of *bceAB*-$FLAG_3$ and
557 *bceS*-His_8 with single-cysteine substitutions and the P_{bceA}-*lux* reporter (SGB369 and
558 derivatives). Starter cultures were grown in 2 ml of LB medium overnight at 37 ºC with
559 agitation, then diluted 1:500 into 55 ml of fresh medium supplemented with 0.02% (w/v)
560 xylose. In mid-exponential growth (OD_{600} 0.5 – 0.7), oxidative cross-linking of cysteine
561 residues was triggered by addition of 250 µM of iodine for 15 min under continued
562 incubation. Where required, cells were induced with 60 µg ml^{-1} Zn^{2+}-bacitracin for 45 min
563 prior to cross-linking. Cross-linking reactions were stopped with 20 mM N-ethylmaleimide
564 (NEM) for 15 min under continued incubation. Cells were harvested by centrifugation (3,000
565 × *g*, 20 min, 4 ºC) and resuspended in 5 ml of ice cold lysis buffer (100 mM Tris-HCl [pH
566 8.0], 150 mM NaCl, 10% (w/v) glycerol, 20 mM NEM). Cell disruption was achieved by at
567 least three cycles of 15s sonication on ice with 15s rest. Debris was removed by
568 centrifugation (3,000 × *g*, 20 min, 4 ºC), and membranes were collected from supernatants by
569 ultracentrifugation (150,000 × *g*, 1 h, 4 ºC). Membranes were resuspended in 50 µl lysis
570 buffer, and approximately 150 mg protein per sample was mixed with non-reducing sample
571 buffer (1× final concentration; 1.5 M Tris/HCl [pH 6.8], 30 % (w/v) glycerol, 350 mM SDS,

572 0.12 mg ml^{-1} bromophenol blue) for SDS-PAGE and Western blot analysis (see below). For
573 quantification of band intensities Fiji (45) was used to obtain a profile plot of each lane, and
574 the relative intensity of each band (monomer and dimer BceS) within the lane was expressed
575 as a percentage of the total band intensities.

576 **Solvent-accessibility of Cysteine residues *in vivo* (Scan-SCAM).** For solvent-accessibility
577 tests in the second transmembrane helix of BceS, the Δ*bceSAB* deletion strain, complemented
578 with xylose-inducible ectopic copies of *bceAB*-$FLAG_3$ and *bceS*-His_8 and the P_{bceA}-*lux*
579 reporter was employed. The *bceS* complementation construct was made cysteine-free via
580 C45S/C198S/C259S substitutions, followed by introduction of single cysteines to be tested
581 (strain SGB936 and derivatives). The same was done in the E115K/K116E variant to assess
582 transmembrane topology in the active state (strain SGB951 and derivatives). Cultures were
583 grown to mid-exponential phase as described above. Cells were harvested, washed twice with
584 50 mM HEPES buffer (pH 6.8) and resuspended in 5 ml of the same buffer. Water exposed
585 (i.e. cytoplasmic) cysteine residues were masked with 40 mM N-Ethylmaleimide (NEM) for
586 1.5 h at room temperature with shaking or left untreated. Masking reactions were stopped by
587 three washes in cold (4 ˚C) 50 mM HEPES buffer (pH 6.8). Cells were resuspended in 5 ml
588 of ice cold lysis buffer, sonicated and membranes collected as above. Membranes were
589 resuspended in 40 µl accessibility buffer (50 mM HEPES [pH 6.8], 1.3% (w/v) SDS).
590 Cysteines that had not been masked with NEM in the first step were labelled with 5 mM
591 methoxypolyethylene glycol maleimide (PEG-mal; Sigma-Aldrich) for 1.5 h at room
592 temperature with agitation. The reaction was stopped with 1× LDS sample buffer (Expedeon)
593 and 250 mM DTT and rested for 5 min. PEG-mal accessible and non-accessible BceS were
594 analyzed by Western Blot.

595 **Western blot analysis.** Protein samples (~150 µg) from *in vivo* cross-linking and Scan-
596 SCAM were subjected to SDS-PAGE on RunBlue™ TEO-Tricine SDS mini gel in either
597 Tris-Tricine-SDS (Sigma-Aldrich) or Teo-Tricine-SDS (Expedeon) buffer, run for 50 min at
598 120V. Samples were transferred to polyvinylidene fluoride (PVDF) membranes (Merck
599 Millipore, activated in 100 % (v/v) methanol) in 1 × RunBlue SDS Running Buffer
600 (Expedeon), 20 % (v/v) methanol at 75 mA for 70 minutes using a PerfectBlue™ Sedec™
601 Semi-Dry Electroblotter (Peqlab). Membranes were blocked with 7.5 % (w/v) skimmed milk
602 powder in PBST (137 mM NaCl, 2.7 mM KCl, 10 mM Na_2HPO_4, 1.8 mM KH_2PO_4 [pH7.4],
603 0.1 % (v/v) Tween 20), washed three times in PBST, and incubated with primary antibody
604 (Penta·His Antibody, QIAGEN®, 1:2000 dilution) in 1% bovine serum albumin in PBST for
605 2h at room temperature. Following three washes in PBST, incubation with secondary
606 antibody (Peroxidase-AffiniPure Goat Anti-Rabbit IgG, Jackson ImmunoResearch Europe
607 Ltd, 1:4000 dilution) was carried out in milk-PBST for 1h at room temperature, followed by
608 three final washes in PBST. Detection of proteins was by chemiluminescence using Pierce™
609 ECL Western Blotting Substrate (Thermo Fisher Scientific Inc.) and a Qiagen CCD camera
610 with Fusion software.

611 **Homology Modelling.** Homology models for the BceS HAMP and DHp domains (positions
612 56 to 174), and for the C-terminal domain of BceAB (from position 507) were generated
613 using I-TASSER with default parameters (29). The respective homology model with the
614 highest C-score was selected, and the top ranking structural analog from PDB identified by I-
615 TASSER was noted for reference.

616 **Gaussian-accelerated molecular dynamics (GaMD) Simulations.** A homology model of
617 the cytoplasmic region of BceS consisting of the DHp and ATPase domains was constructed
618 using I-TASSER as before (46). The HAMP-like domain was excluded due to low sequence

619 homology with conventional HAMP domains. The approximate orientation of each BceS
620 monomer with respect to one another was predicted based on cysteine cross-linking data (Fig.
621 2) and further refined using Z-Dock to perform rigid body protein-protein docking (47), with
622 subsequent side chain rotamers optimised using SCWRL4 (48). The N-terminus of the DHp
623 domain of each monomer was acetylated to cap the α-helix and prevent having a positive
624 charge at the termini. ATP was then docked into each ATP binding site using AutoDock Vina
625 (exhaustiveness set to 32) (49). The generated model of BceS was then manually modified to
626 construct the E115K/K116E variant. All residues were modelled in their standard protonation
627 states, with His108 and His124 singly protonated on the Nδ1 nitrogen, and all other His
628 singly protonated on the Nε2 nitrogen (as indicated by hydrogen bonding networks). Both
629 systems were solvated in an octahedral water box such that no protein/substrate atom was
630 within 10 Å of the box boundaries, with Na^+ or Cl^- counter ions added as necessary to ensure
631 an overall neutral charge. MD simulations were performed using GPU accelerated Amber16,
632 with the ff14SB force field and TIP3P water model used to describe protein and water
633 molecules respectively. Parameters for ATP were taken from a study by Meagher and
634 colleagues (50). Following a minimisation, heating, NVT and NPT equilibration procedure
635 (described below), Gaussian accelerated MD (GaMD) simulations were done in the NVT
636 ensemble at 300 K (31), with a boost potential applied to both the total system potential
637 energy as well as the dihedral potential energies (see also GaMD settings in Table S5). To
638 prepare for production GaMD simulations, a 12 ns long conventional MD run was used to
639 obtain maximum, minimum, average and standard deviation of the system potential energies.
640 Following this, a 66 ns long run was used to update the above parameters (updated every 600
641 ps) to ensure converged GaMD production parameters. Production GaMD simulations were
642 then run for 4 × 500 ns, using different random seeds for each replica. MD simulations were
643 run using a 2 fs time step with the SHAKE algorithm applied to any bond containing a

644 hydrogen atom. An 8 Å direct space non-bonded cut-off was applied with long-range
645 electrostatics evaluated using the particle mesh Ewald algorithm (51). Temperature was
646 regulated using Langevin temperature control (collision frequency of 1 ps^{-1}). All MD and
647 GaMD simulations were performed with a 10 kcal mol^{-1} restraint on the Phi and Psi dihedrals
648 between the acetyl and first N-terminal residue, to prevent the α-helix fraying. Principal
649 component analysis (PCA) and other trajectory analyses were performed within CPPTRAJ
650 (52), on the Cα atoms of the DHp domain residues. PCA was performed on the trajectories
651 after constructing an average structure of all four simulations combined. Reweighting of PCA
652 and distance measurements (to obtain PMFs) was performed using the 'PyReweighting'
653 toolkit (53).
654 To equilibrate structures for GaMD simulations, the following procedure was performed.
655 Minimisation of all hydrogen atoms and solvent molecules was done using 500 steps of
656 steepest descent followed by 500 steps of conjugate gradient. To keep all other atoms (i.e. the
657 protein heavy atoms) in place during the minimisation, 10 kcal mol^{-1} $Å^{-1}$ positional restraints
658 were applied. Retaining the positional restraints on all protein heavy atoms, the system was
659 then heated rapidly from 50 K to 300 K in the NVT ensemble over the course of 200 ps. This
660 system was again minimised for a further 500 steps of steepest descent followed by 500 steps
661 of conjugate gradient, this time only applying positional restraints (of size 5 kcal mol^{-1} $Å^{-1}$)
662 to the Cα carbon atoms. These Cα restraints were retained as the system was again heated
663 from 25 K to 300 K over the course of 50 ps in the NVT ensemble. Simulations were then
664 performed in the NPT ensemble (1 atm, 300 K), first gradually reducing the 5 kcal mol^{-1} $Å^{-1}$
665 Cα carbon restraints over the course of 50 ps of simulation time. This was done in five steps
666 (5, 4, 3, 2, 1 kcal mol^{-1} $Å^{-1}$) of 10 ps each. A final 20 ns long MD simulation was then
667 performed, in which no restraints were used, to equilibrate the box size. All dynamics steps
668 used the SHAKE algorithm. Simulations performed in the NVT ensemble used Langevin

temperature control (with a collision frequency of 1 ps^{-1}) and a simulation time-step of 1 fs. Simulations performed in the NPT ensemble again used Langevin temperature control (collision frequency of 1 ps^{-1}) and a Berendsen barostat (1 ps pressure relaxation time), with a simulation time-step of 2 fs.

ACKNOWLEDGEMENTS

The authors thank Roger Draheim for helpful advice in establishing the cysteine crosslinking assays. We also thank our undergraduate research students Jessica Lancaster and Adam McCartan for constructing plasmids pJL705 and pAM703, respectively. We thank Jean van den Elsen and Laurence Hurst for critical reading of and feedback on the manuscript.

Work in SG's lab was supported by the Biotechnology and Biological Sciences Research Council (BBSRC; BB/M029255/1). MWK is a BBSRC David Phillips Fellow (BB/M026280/1).

AUTHOR CONTRIBUTIONS

AK and MJG carried out all laboratory work and data analysis; MWK and CRP performed and analyzed the MD simulations; SG supervised all laboratory work and coordinated the research project; SG, CRP and AK wrote the manuscript.

REFERENCES

1. **Waglechner N**, **Wright GD**. 2017. Antibiotic resistance: it's bad, but why isn't it worse? BMC Biol **15**:1–8.

2. **Durão P**, **Balbontín R**, **Gordo I**. 2018. Evolutionary Mechanisms Shaping the Maintenance of Antibiotic Resistance. Trends Microbiol **26**:677–691.

692 3. **Andersson DI**, **Hughes D**. 2010. Antibiotic resistance and its cost: is it possible to
693 reverse resistance? Nat Rev Microbiol **8**:260–271.

694 4. **Fritz G**, **Dintner S**, **Treichel NS**, **Radeck J**, **Gerland U**, **Mascher T**, **Gebhard S**.
695 2015. A new way of sensing: need-based activation of antibiotic resistance by a flux-
696 sensing mechanism. mBio **6**:e00975–15.

697 5. **Dintner S**, **Heermann R**, **Fang C**, **Jung K**, **Gebhard S**. 2014. A sensory complex
698 consisting of an ATP-binding cassette transporter and a two-component regulatory
699 system controls bacitracin resistance in *Bacillus subtilis*. J Biol Chem **289**:27899–
700 27910.

701 6. **Staroń A**, **Finkeisen DE**, **Mascher T**. 2011. Peptide antibiotic sensing and
702 detoxification modules of *Bacillus subtili*s. Antimicrob Agents Chemother **55**:515–
703 525.

704 7. **Hiron A**, **Falord M**, **Valle J**, **Débarbouillé M**, **Msadek T**. 2011. Bacitracin and nisin
705 resistance in *Staphylococcus aureus*: a novel pathway involving the BraS/BraR two-
706 component system (SA2417/SA2418) and both the BraD/BraE and VraD/VraE ABC
707 transporters. Mol Microbiol **81**:602–622.

708 8. **Dintner S**, **Staroń A**, **Berchtold E**, **Petri T**, **Mascher T**, **Gebhard S**. 2011.
709 Coevolution of ABC transporters and two-component regulatory systems as resistance
710 modules against antimicrobial peptides in Firmicutes bacteria. J Bacteriol **193**:3851–
711 3862.

712 9. **Revilla-Guarinos A**, **Gebhard S**, **Alcántara C**, **Staroń A**, **Mascher T**, **Zúñiga M**.
713 2013. Characterization of a regulatory network of peptide antibiotic detoxification
714 modules in *Lactobacillus casei* BL23. Appl Environ Microbiol **79**:3160–3170.

715 10. **Gebhard S**, **Fang C**, **Shaaly A**, **Leslie DJ**, **Weimar MR**, **Kalamorz F**, **Carne A**,
716 **Cook GM**. 2014. Identification and Characterization of a Bacitracin Resistance
717 Network in *Enterococcus faecalis*. Antimicrob Agents Chemother **58**:1425–1433.

718 11. **Ouyang J**, **Tian XL**, **Versey J**, **Wishart A**, **Li YH**. 2010. The BceABRS Four-
719 Component System Regulates the Bacitracin-Induced Cell Envelope Stress Response
720 in *Streptococcus mutans*. Antimicrob Agents Chemother **54**:3895–3906.

721 12. **Gebhard S**, **Mascher T**. 2011. Antimicrobial peptide sensing and detoxification
722 modules: unravelling the regulatory circuitry of *Staphylococcus aureus*. Mol Microbiol
723 **81**:581–587.

724 13. **Revilla-Guarinos A**, **Gebhard S**, **Mascher T**, **Zúñiga M**. 2014. Defence against
725 antimicrobial peptides: different strategies in Firmicutes. Environ Microbiol **16**:1225–
726 1237.

727 14. **Gebhard S**. 2012. ABC transporters of antimicrobial peptides in Firmicutes bacteria -
728 phylogeny, function and regulation. Mol Microbiol **86**:1295–1317.

729 15. **Greene NP**, **Kaplan E**, **Crow A**, **Koronakis V**. 2018. Antibiotic Resistance Mediated
730 by the MacB ABC Transporter Family: A Structural and Functional Perspective. Front
731 Microbiol **9**:1923–17.

732 16. **Kobras CM**, **Piepenbreier H**, **Emenegger J**, **Sim A**, **Fritz G**, **Gebhard S**. 2020.
733 BceAB-Type Antibiotic Resistance Transporters Appear To Act by Target Protection
734 of Cell Wall Synthesis. Antimicrob Agents Chemother **64**:321–15.

735 17. **Gao R**, **Stock AM**. 2009. Biological insights from structures of two-component
736 proteins. Annu Rev Microbiol **63**:133–154.

737 18. **Gushchin I**, **Melnikov I**, **Polovinkin V**, **Ishchenko A**, **Yuzhakova A**, **Buslaev P**,
738 **Bourenkov G**, **Grudinin S**, **Round E**, **Balandin T**, **Borshchevskiy V**, **Willbold D**,
739 **Leonard G**, **Büldt G**, **Popov A**, **Gordeliy V**. 2017. Mechanism of transmembrane
740 signaling by sensor histidine kinases. Science **356**:eaah6345–9.

741 19. **Bhate MP**, **Molnar KS**, **Goulian M**, **DeGrado WF**. 2015. Signal Transduction in
742 Histidine Kinases: Insights from New Structures. Structure/Folding and Design
743 **23**:981–994.

744 20. **Bhate MP**, **Lemmin T**, **Kuenze G**, **Mensa B**, **Ganguly S**, **Peters JM**, **Schmidt N**,
745 **Pelton JG**, **Gross CA**, **Meiler J**, **DeGrado WF**. 2018. Structure and Function of the
746 Transmembrane Domain of NsaS, an Antibiotic Sensing Histidine Kinase in
747 *Staphylococcus aureus*. J Am Chem Soc **140**:7471–7485.

748 21. **Monzel C**, **Unden G**. 2015. Transmembrane signaling in the sensor kinase DcuS of
749 *Escherichia coli*: A long-range piston-type displacement of transmembrane helix 2.
750 Proc Natl Acad Sci USA **112**:11042–11047.

751 22. **Tetsch L**, **Jung K**. 2009. The regulatory interplay between membrane-integrated
752 sensors and transport proteins in bacteria. Mol Microbiol **73**:982–991.

753 23. **Piepenbreier H**, **Fritz G**, **Gebhard S**. 2017. Transporters as information processors in
754 bacterial signalling pathways. Mol Microbiol **104**:1–15.

755 24. **Witan J**, **Bauer J**, **Wittig I**, **Steinmetz PA**, **Erker W**, **Unden G**. 2012. Interaction of
756 the *Escherichia coli* transporter DctA with the sensor kinase DcuS: presence of
757 functional DctA/DcuS sensor units. Mol Microbiol **85**:846–861.

758 25. **Unden G**, **Wörner S**, **Monzel C**. 2016. Cooperation of secondary transporters and
759 sensor kinases in transmembrane signalling: the DctA/DcuS and DcuB/DcuS sensor
760 complexes of *Escherichia coli*. Adv Microb Physiol **68**:139–167.

761 26. **Hsieh Y-J**, **Wanner BL**. 2010. Global regulation by the seven-component P_i signaling
762 system. Curr Opin Microbiol **13**:198–203.

763 27. **Rietkötter E**, **Hoyer D**, **Mascher T**. 2008. Bacitracin sensing in *Bacillus subtilis*. Mol
764 Microbiol **68**:768–785.

765 28. **Letunic I**, **Doerks T**, **Bork P**. 2012. SMART 7: recent updates to the protein domain
766 annotation resource. Nucleic Acids Res **40**:D302–5.

767 29. **Zhang Y**. 2008. I-TASSER server for protein 3D structure prediction. BMC
768 Bioinformatics, 2nd ed. **9**:76–8.

769 30. **Pakula AA**, **Simon MI**. 1992. Determination of transmembrane protein structure by
770 disulfide cross-linking: the *Escherichia coli* Tar receptor. Proc Natl Acad Sci USA
771 **89**:4144–4148.

772 31. **Miao Y**, **Feher VA**, **McCammon JA**. 2015. Gaussian Accelerated Molecular
773 Dynamics: Unconstrained Enhanced Sampling and Free Energy Calculation. J Chem
774 Theory Comput **11**:3584–3595.

775 32. **Lai R-Z**, **Parkinson JS**. 2014. Functional Suppression of HAMP Domain Signaling
776 Defects in the *E. coli* Serine Chemoreceptor. J Mol Biol **426**:3642–3655.

777 33. **Hulko M**, **Berndt F**, **Gruber M**, **Linder JU**, **Truffault V**, **Schultz A**, **Martin J**,
778 **Schultz JE**, **Lupas AN**, **Coles M**. 2006. The HAMP Domain Structure Implies Helix
779 Rotation in Transmembrane Signaling. Cell **126**:929–940.

780 34. **Zhou Q**, **Ames P**, **Parkinson JS**. 2011. Biphasic control logic of HAMP domain
781 signalling in the *Escherichia coli* serine chemoreceptor. Mol Microbiol **80**:596–611.

782 35. **Ferris HU**, **Dunin-Horkawicz S**, **Mondéjar LG**, **Hulko M**, **Hantke K**, **Martin J**,
783 **Schultz JE**, **Zeth K**, **Lupas AN**, **Coles M**. 2011. The Mechanisms of HAMP-
784 Mediated Signaling in Transmembrane Receptors. Structure/Folding and Design
785 **19**:378–385.

786 36. **Ferris HU**, **Dunin-Horkawicz S**, **Hornig N**, **Hulko M**, **Martin J**, **Schultz JE**, **Zeth**
787 **K**, **Lupas AN**, **Coles M**. 2012. Mechanism of Regulation of Receptor Histidine
788 Kinases. Structure/Folding and Design **20**:56–66.

789 37. **Matamouros S**, **Hager KR**, **Miller SI**. 2015. HAMP Domain Rotation and Tilting
790 Movements Associated with Signal Transduction in the PhoQ Sensor Kinase. mBio
791 **6**:e00616–15.

792 38. **Appleman JA**, **Stewart V**. 2003. Mutational Analysis of a Conserved Signal-
793 Transducing Element: the HAMP Linker of the *Escherichia coli* Nitrate Sensor NarX.
794 J Bacteriol **185**:89–97.

795 39. **Crow A**, **Greene NP**, **Kaplan E**, **Koronakis V**. 2017. Structure and
796 mechanotransmission mechanism of the MacB ABC transporter superfamily. Proc
797 Natl Acad Sci USA **23**:201712153–6.

798 40. **Kallenberg F**, **Dintner S**, **Schmitz R**, **Gebhard S**. 2013. Identification of regions
799 important for resistance and signalling within the antimicrobial peptide transporter
800 BceAB of *Bacillus subtilis*. J Bacteriol **195**:3287–3297.

801 41. **Ho SN**, **Hunt HD**, **Horton RM**, **Pullen JK**, **Pease LR**. 1989. Site-directed
802 mutagenesis by overlap extension using the polymerase chain reaction. Gene **77**:51–
803 59.

804 42. **Harwood CR**, **Cutting SM**. 1990. Molecular biological methods for *Bacillus*. John
805 Wiley & Sons, Chichester, UK.

806 43. **Arnaud M**, **Chastanet A**, **Débarbouillé M**. 2004. New vector for efficient allelic
807 replacement in naturally nontransformable, low-GC-content, Gram-positive bacteria.
808 Appl Environ Microbiol **70**:6887–6891.

809 44. **Radeck J**, **Kraft K**, **Bartels J**, **Cikovic T**, **Dürr F**, **Emenegger J**, **Kelterborn S**,
810 **Sauer C**, **Fritz G**, **Gebhard S**, **Mascher T**. 2013. The *Bacillus* BioBrick Box:
811 generation and evaluation of essential genetic building blocks for standardized work
812 with *Bacillus subtilis*. Journal of Biological Engineering **7**:29.

813 45. **Schindelin J**, **Arganda-Carreras I**, **Frise E**, **Kaynig V**, **Longair M**, **Pietzsch T**,
814 **Preibisch S**, **Rueden C**, **Saalfeld S**, **Schmid B**, **Tinevez J-Y**, **White DJ**, **Hartenstein**
815 **V**, **Eliceiri K**, **Tomancak P**, **Cardona A**. 2012. Fiji: an open-source platform for
816 biological-image analysis. Nature Publishing Group **9**:676–682.

817 46. **Yang J**, **Yan R**, **Roy A**, **Xu D**, **Poisson J**, **Zhang Y**. 2015. The I-TASSER Suite:
818 protein structure and function prediction. Nature Publishing Group **12**:7–8.

819 47. **Pierce BG**, **Wiehe K**, **Hwang H**, **Kim B-H**, **Vreven T**, **Weng Z**. 2014. ZDOCK
820 server: interactive docking prediction of protein-protein complexes and symmetric
821 multimers. Bioinformatics **30**:1771–1773.

822 48. **Krivov GG**, **Shapovalov MV**, **Dunbrack RL**. 2009. Improved prediction of protein
823 side-chain conformations with SCWRL4. Proteins **77**:778–795.

824 49. **Trott O**, **Olson AJ**. 2010. AutoDock Vina: improving the speed and accuracy of
825 docking with a new scoring function, efficient optimization, and multithreading. J
826 Comput Chem **31**:455–461.

827 50. **Meagher KL**, **Redman LT**, **Carlson HA**. 2003. Development of polyphosphate
828 parameters for use with the AMBER force field. J Comput Chem **24**:1016–1025.

829 51. **Darden T**, **York D**, **Pedersen L**. 1993. Particle mesh Ewald: An N·log(N) method
830 for Ewald sums in large systems. The Journal of Chemical Physics **98**:10089–10092.

831 52. **Roe DR**, **Cheatham TE III**. 2013. PTRAJ and CPPTRAJ: Software for Processing
832 and Analysis of Molecular Dynamics Trajectory Data. J Chem Theory Comput
833 **9**:3084–3095.

834 53. **Miao Y**, **Sinko W**, **Pierce L**, **Bucher D**, **Walker RC**, **McCammon JA**. 2014.
835 Improved Reweighting of Accelerated Molecular Dynamics Simulations for Free
836 Energy Calculation. J Chem Theory Comput **10**:2677–2689.

837

838 **FIGURE LEGENDS**

839 **Figure 1. Function of the BceRS-BceAB resistance system of *B. subtilis.*** BceS and its
840 domains are shown in shades of blue, with the HAMP-like domain in dark turquoise, and
841 DHp domain in dark blue. Only a single monomer of BceS is shown for clarity. BceAB is in
842 green with the 8th transmembrane helix marked in dark green; the A_2B stoichiometry is
843 shown (5), and the extracellular domain indicated by a U-shaped black line. The left section
844 of the schematic shows the system in its inactive (OFF) state, and the repressing function of
845 the transporter indicated by a red blunt arrow. The right shows the active (ON) state in the
846 presence of antibiotics, exemplified by bacitracin, with the activating function of the
847 transporter shown as a red lightning bolt. The motions of kinase domains upon activation are
848 shown as red block arrows and BceS autophosphorylation by a 'P'. The positioning of the
849 symbols within the sensory complex for repression/activation is arbitrary. ATP hydrolysis
850 reactions and antibiotic removal are indicated by grey arrows; for simplicity ATP hydrolysis
851 is only shown for one ATPase.

852

853 **Figure 2: BceS DHp domain forms a four-helix bundle. a**, Homology model of the BceS
854 HAMP-like and DHp domains generated by I-TASSER (C-score = -0.76). The HAMP-like
855 domain is shown in purple and the DHp domain in blue. The residues that form Cys-
856 crosslinks in panel b are highlighted, E115 (red), E118 (purple) and L119 (green). Residue
857 K167, which sits opposite E115, is shown in orange. **b**, Percentage of crosslinking for each
858 BceS Cys variant was calculated from relative band intensities between monomer and dimer
859 within each lane using Fiji (45). Amino acid substitutions were introduced in parent construct
860 *bceS*^{WT}-His$_8$ (SGB369) and BceS production was controlled by addition of 0.02 % (w/v)
861 xylose. Data are shown as mean ± SD from 2-5 independent repeats. **c, d**, Schematic diagram

862 of the BceS DHp dimer configuration. Helices labelled DHp1' and DHp2' show the second
863 protomer. Left, top down view of the helices in the structural model; right, helical wheel
864 diagram of the top two helical turns in the DHp domain; residues that form crosslinks are
865 highlighted as before.

866

867 **Figure 3: Charges within the BceS DHp domain core affect kinase activity. a,** BceS
868 signaling activity in strains harbouring P_{bceA}-*luxABCDE* and P_{xyl}-*bceS*. Amino acid
869 substitutions were introduced in parent construct $bceS^{WT}$-His_8 (SGB369). Signaling was
870 induced with 1µg ml^{-1} of bacitracin. Data are shown as mean ± SD from 4-22 biological
871 repeats. The schematic below shows the location of individual and net charges in the core and
872 stabilisation points within the four-helix bundle, as illustrated in panel b. Red, positive
873 charge; orange, negative charge. **b**, Helical wheel diagram of the top two helical turns in the
874 DHp dimer configuration showing location of charges and stabilisation points (pink and
875 cyan). Helices labelled DHp1' and DHp2' show the second protomer. Black curve arrows
876 denote the direction of helical rotation. **c**, 2D plots of potential of mean force (PMF) obtained
877 in GaMD simulations of the wild type (WT, left) and E115K/K116E variant (right) protein.
878 Inter-monomer distances shown are between the Cα carbon atoms of residues at positions
879 115 (x-axes) and 167 (y-axes). The PMFs are projected onto the surface in kcal mol^{-1}
880 indicated by the heat scale.

881

882 **Figure 4: BceS contains a HAMP-like signal transfer domain. a**, Sequence alignment of
883 known HAMP domains and the BceS HAMP-like domain generated with ClustalO. Residues
884 in red form the packing layers in the Af1503 HAMP domain. The black solid arrow indicates
885 the packing residue that influences signaling state in some HAMP domains. White open

886 arrows indicate E60 and F63 critical for BceS function. Proteins included and their GenBank
887 identifiers are Af1503 (O28769), BceS (BSU30390), PhoQ (P23837), CpxA (P0AE82),
888 EnvZ (P0AEJ4), NarX (P0AFA2), Tsr (P02942), Tar (P07017), Aer (P50466). **b**, Schematic
889 showing amino acids and their sizes in MW used in size substitutions. **c**, BceS signaling
890 activity following L67 amino acid size substitution harbouring P_{bceA}-*luxABCDE* and P_{xyl}-
891 *bceS*. Amino acid substitutions were introduced in the parent construct $bceS^{WT}$-His_8
892 (SGB369). Signaling was induced with 1µg ml^{-1} of bacitracin. Data are shown as mean ± SD
893 from 5-18 biological repeats. **d**, Helical wheel diagram of the HAMP-like domain. Individual
894 helices are abbreviated HL-1 and HL-2; the labels HL-1' and HL-2' show the second
895 protomer. Residues essential for BceS activity are E60 (red) and F63 (yellow); the key
896 packing residue L67 is shown in blue; red/blue semicircles are used to indicate positioning of
897 residues in subsequent helical layers. **e**, BceS signaling activity of the constitutive ON variant
898 ($BceS^{E115K}$) combined with loss-of-function substitutions at positions 60 and 63. Amino acid
899 substitutions were introduced in parent construct $bceS^{WT}$-His_8 (SGB401). Signaling in cells
900 harbouring P_{bceA}-*lacZ* and P_{xyl}-*bceS* was induced with 1µg ml^{-1} of bacitracin, BceS production
901 was controlled by addition of 0.02 % (w/v) xylose. Data are shown as mean ± SD from 3-7
902 biological repeats. The inset shows an anti-His Western blot analysis to confirm membrane
903 localisation and protein levels of wild-type (WT) BceS and its variants.

904

905 **Figure 5: Accessibility of Cys residues at the membrane interface shows a piston-like**
906 **displacement upon BceS activation. a,** Schematic representation of transmembrane helix 2
907 in the OFF and ON states, respectively. Relevant native amino acids are indicated in one-
908 letter code. Solvent-accessible (PEGylated) Cys replacements are shown in blue, inaccessible
909 (unPEGylated) Cys replacements in red and residues not tested in white. Residues circled in

910 black were tested in triplicate, those circled in grey in duplicate. **b**, Anti-His Western blot
911 analysis of solvent-accessibility of Cys replacements (Scan-SCAM). Bands corresponding to
912 PEGylated (S-PEG) and unmodified (S) BceS are indicated; individual lanes are outlined in
913 the same colour code as used in panel a. 'Cys-less' indicates the parent variant of BceS
914 lacking its native Cys residues. OFF state: amino acids substituted in parent construct
915 *bceS*$^{C45S/C198S/C259S}$-His$_8$ (SGB936). ON state: amino acids substituted in parent construct
916 *bceS*$^{E115K/K116E/C45S/C198S/C259S}$-His$_8$ (SGB951).

917

918 **Figure 6: Control of BceS activity by the transporter BceAB. a,** Signaling activity of
919 BceS measured in strains harbouring P$_{bceA}$-*luxABCDE* and challenged with 10µg ml^{-1} of
920 bacitracin (grey) or left untreated (black). Amino acid substitutions were introduced into
921 parent construct P$_{xyl}$-*bceS*-His$_8$, in a strain background carrying a Δ*bceS* deletion (BceAB +;
922 SGB792), or a Δ*bceSAB* deletion (BceAB -; SGB818). Data are shown as mean ± SD from 5-
923 12 biological repeats. **b,** Signaling phenotype of BceAB variants. Amino acid substitutions
924 were introduced into the P$_{xyl}$-*bceAB*-FLAG$_3$ parent construct, and signaling assessed using
925 either a P$_{bceA}$-*lacZ* (SGB370 and derivatives) or P$_{bceA}$-*luxABCDE* (SGB731 and derivatives)
926 reporter. Cells were challenged with a series of bacitracin concentrations, and the lowest
927 concentration giving signaling above background is shown by circles in the plot (see Fig. S7
928 for complete datasets). Analyses were based on mean values from at least three independent
929 repeats. The first line of x-axis labels gives native amino acids, the lines below indicate
930 substitutions tested. The bar above the graph shows positions in the BceB sequence and areas
931 within the membrane (grey bar) or in the cytoplasm (black line). Circle colours are assigned
932 green, wild-type (WT) signaling threshold; red, increased signaling threshold; blue, reduced
933 signaling threshold.

934 **LIST OF SUPPLEMENTAL FILES**

935 **Figure S1.** Cysteine scanning and site-directed mutagenesis of the BceS DHp domain.

936 **Figure S2.** Cysteine cross-linking following activation of signaling.

937 **Figure S3.** Equilibration and principle component analysis of Gaussian accelerated molecular
938 dynamics simulations of BceS DHp domain conformation.

939 **Figure S4.** Cysteine scanning mutagenesis of the BceS HAMP-like domain.

940 **Figure S5.** Cysteine scanning mutagenesis of the second transmembrane helix of BceS.

941 **Figure S6.** Arginine substitutions in transmembrane helix 2 of BceS.

942 **Figure S7.** Signaling phenotypes of BceAB variants.

943

944 **SI Experimental procedures.**

945 **Table S1.** Strains used in this study

946 **Table S2.** Primers used in this study

947 **Table S3.** Plasmids used in this study

948 **Table S4.** Minimal inhibitory concentration of bacitracin in strains carrying BceAB variants

949 **Table S5.** Parameters used for GaMD simulations